

MATERIALS SCIENCE

Switchable counterion gradients around charged metallic nanoparticles enable reception of radio waves

Xing Zhao^{1,2*}, Bin Tu^{3*}, Mengyao Li^{1,4}, Xiaojing Feng¹, Yuchun Zhang¹, Qiaojun Fang³, Tiehu Li², Bartosz A. Grzybowski^{5,6†}, Yong Yan^{1†}

Mechanically flexible, easy-to-process, and environmentally benign materials capable of current rectification are interesting alternatives to “hard” silicon-based devices. Among these materials are metallic/charged-organic nanoparticles in which electronic currents through metal cores are modulated by the gradients of counterions surrounding the organic ligands. Although layers of oppositely charged particles can respond to both electronic and chemical signals and can function even under significant mechanical deformation, the rectification ratios of these “chemoelectronic” elements have been, so far, low. This work shows that significantly steeper counterion gradients and significantly higher rectification ratios can be achieved with nanoparticles of only one polarity but in contact with a porous electrode serving as a counterion “sink.” These composite structures act as rectifiers even at radio frequencies, providing a new means of interfacing counterions’ dynamics with high-frequency electronic currents.

INTRODUCTION

Although modern electronics is based predominantly on semiconducting materials (1, 2), electronic circuits can also be prepared from conductors confined to nanoscopic dimensions (3–5). For instance, in films of metallic nanoparticles (NPs) functionalized with charged organic ligands (6), the flow of electrons through the jammed metal cores can be modulated by the concentration gradients of the surrounding mobile counterions (7). In our previous works (7, 8), we showed that when thin layers (~0.5 μm) of oppositely charged NPs are stacked, counterion concentration gradients near the interfacial region give rise to an internal electric field, allowing these sandwich structures to act as diodes and integral components of all metal-NP circuits capable of processing both electronic and chemical signals. Although these “chemoelectronic” circuits offer mechanical flexibility and the ease of “green” fabrication (i.e., the NPs themselves are environmentally benign and the particle layers are simply cast from alcoholic solutions under ambient conditions), lamination of bilayer NP diodes without shorting may be challenging, while their current rectification performance is limited by the bilayer thickness and by the degree to which counterions near the interfacial region can interdiffuse to set up local concentration gradients. In an effort to make these gradients steeper, and the rectification ratios of the diodes higher, one has to consider two effects: On one hand, it is desirable to “strip” from the NPs as many counterions as possible, and on the other hand, concentrating these counterions in some regions of the NP layer between impenetrable solid electrodes is energetically unfavorable. We hypothesized that these opposing tendencies can be reconciled by

changing not the properties of the particles (as we attempted earlier) but of the electrodes flanking them. In particular, if one of these electrodes were made porous, then it could absorb more counterions with much less energetic penalty. Here, we verify this hypothesis and demonstrate that significantly more robust and efficient current rectification can be achieved with NPs of only one polarity but sandwiched between asymmetric electrodes, one of which is highly porous and can act as counterion “sink” (Fig. 1A). Compared to the earlier bilayer designs (see fig. S4), our one-NP-type diodes exhibit significantly higher rectification ratios (~50 versus ~5 before) with shorter response times (tens versus hundreds of milliseconds to reach steady-state values). On the basis of these properties, we demonstrate a half-wave metal NP-based rectifier with which we intercept, demodulate, and converted into sound 510-kHz radio signals (e.g., some of Mozart’s compositions in supplementary audio files). Beyond current work, the ability to interface radio signals with counterion motions can provide new means to study the dynamics of ionic atmospheres and to probe reactions [affecting these counterions (8)] on and around charged nano-objects.

RESULTS

To fabricate “one-NP-type diodes,” a thin, ~500-nm layer composed of AuNPs 5.6±0.8 nm in diameter and covered with a shell of positively charged *N,N,N*-trimethyl(11-mercaptoundecyl)ammonium chloride (HS-C₁₁NMe₃⁺Cl⁻; TMA) ligands (6, 9) was cast from methanolic solution against a nanoporous electrode made of single-walled carbon nanotubes and graphene (CNTs/graphene) (Fig. 1A). The electrode itself was made by filtering an aqueous dispersion of 0.001 weight % (wt %) graphene and 0.002 wt % single-walled carbon nanotube (SWNT) solutions through a mixed cellulose ester (MCE) polymeric membrane (0.22 μm, 40 mm in diameter), washing and transferring the as-prepared film from this membrane onto a silica substrate, and annealing at 300°C to remove extra solvent, ultimately producing a porous layer (depending on the volumes of solutions used, ~20 to 80 nm thick; see fig. S1B) shown in the scanning electron microscopy (SEM) image in the bottom left part of Fig. 1A (also see fig. S1A) (10). A ~500-nm film of TMA AuNPs was also deposited onto a 40-nm-thick film of gold e-beam evaporated on a silica substrate. CNT/graphene//Au TMA

¹CAS Key Laboratory of Nanosystem and Hierarchical Fabrication, CAS Center for Excellence in Nanoscience, National Center for Nanoscience and Technology, Beijing 100190, China. ²School of Materials Science and Engineering, Northwestern Polytechnical University, Xi’an 710072, China. ³CAS Key Laboratory for Biomedical Effects of Nanomaterials and Nanosafety, CAS Center for Excellence in Nanoscience, National Center for Nanoscience and Technology, Beijing 100190, China. ⁴University of Chinese Academy of Sciences, Beijing 100049, China. ⁵Institute of Organic Chemistry, Polish Academy of Sciences, Ulica Kasprzaka 44/52, Warsaw 02-224, Poland. ⁶IBS Center for Soft and Living Matter and Department of Chemistry, UNIST, 50 UNIST-gil, Eonyang-eup, Ulsan-gun, Ulsan 44919, South Korea.

*These authors contributed equally to this work.

†Corresponding author. Email: nanogrzybowski@gmail.com (B.A.G.); yany@nanocr.cn (Y.Y.)

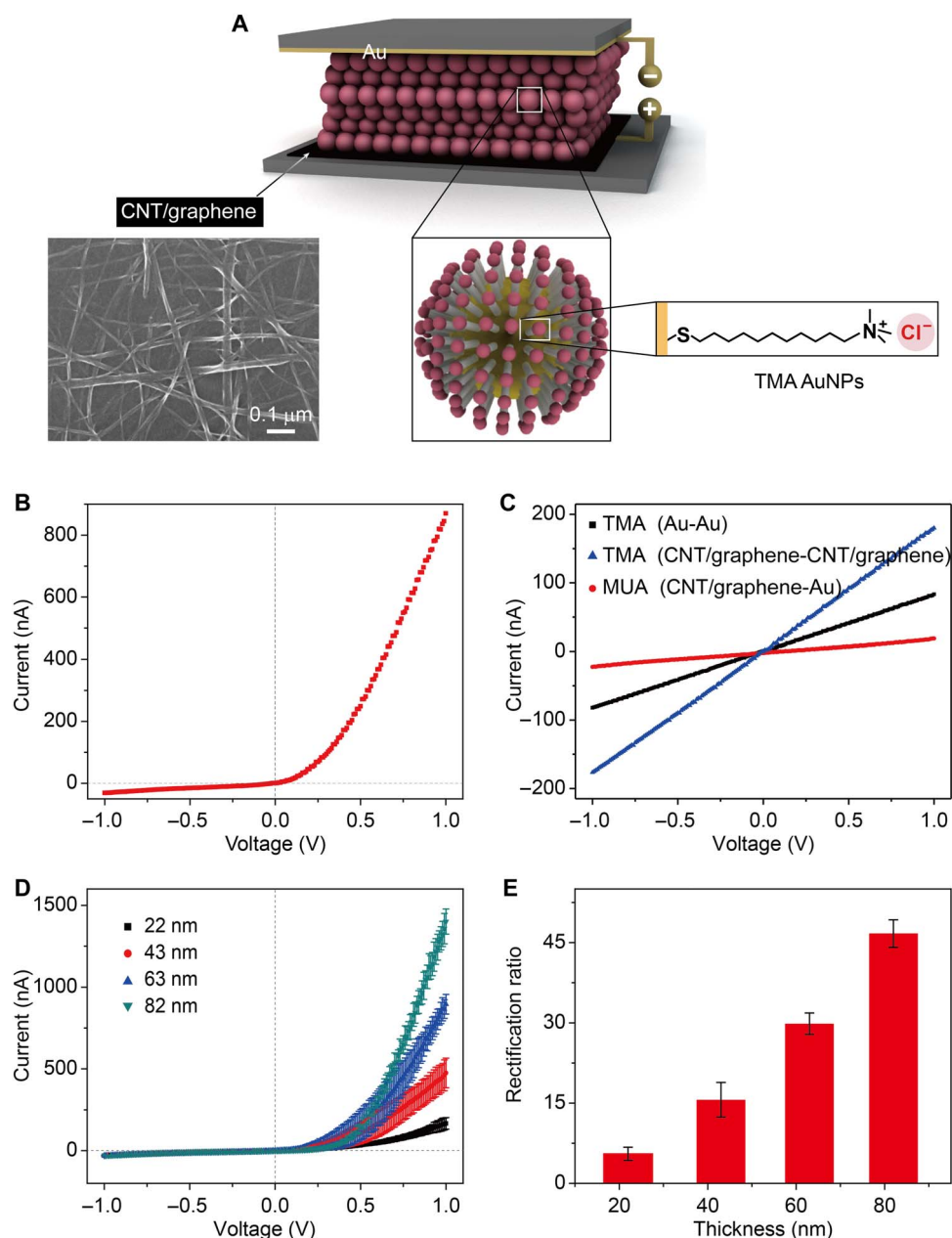


Fig. 1. Device architecture and its current rectification characteristics at steady state. (A) Scheme of the device in which a $\sim 1\text{-}\mu\text{m}$ -thick layer of AuNPs functionalized with charged HS-(CH₂)₁₁-N(CH₃)₃⁺Cl (TMA) ligands is flanked by a gold electrode and a porous CNT/graphene electrode. The SEM image shows the microstructure of the CNT/graphene electrode. The scheme of the NP and of the individual thiol (along with the mobile counterion) is also shown. (B) Typical current-voltage characteristics of the device collected at a sweep rate of 0.01 V/s. With a positive bias placed on the CNT/graphene electrode, the current increases rapidly and the rectification ratio ($r = |I_{+1\text{V}}/I_{-1\text{V}}|$) reaches ~ 30 . (C) Linear current-voltage characteristics recorded for TMA AuNPs flanked by symmetric electrodes (Au-Au and CNT/graphene-CNT/graphene) and for protonated, electrically neutral MUA AuNPs flanked by asymmetric, Au-CNT/graphene-Au. (D) Current-voltage characteristics for devices varying in the thickness of the CNT/graphene electrode (from ~ 20 to ~ 80 nm). Error bars are based on six independent devices. The curves were normalized to have the same current at -1 V. (E) Plotted corresponding rectification ratios.

and Au//Au TMA NP films were then laminated face-to-face, and the entire assembly was encased in polydimethylsiloxane (PDMS). All measurements were performed in a hermetically sealed, homemade Faraday cage using a computer-interfaced Keithley 6517 high-precision electrometer. For further synthetic and fabrication details, see the supplementary materials.

The current-voltage (I - V) characteristics plotted in Fig. 1B evidence that the CNT/graphene//Au TMA//Au laminate rectifies current efficiently, with rectification ratios $r = |I_{+1\text{V}}/I_{-1\text{V}}|$ around 30 at both fast (100 mV s^{-1}) and slow (1 mV s^{-1}) sweep rates. The presence of counterions is essential to achieve rectification, as $r = 1$ when AuNPs functionalized with neutral ligands are used [see the red line in Fig. 1C for

protonated 11-mercaptoundecanoic acid (MUA) ligands] or when CNT/graphene and Au electrodes are put in direct contact, without any NPs in between (fig. S2A). Furthermore, the fact that the electrodes are asymmetric is important ($r = 1$ for AuTMAs flanked by either two Au or two CNT/graphene electrodes; see black and blue lines in Fig. 1C) and so is the porosity of the CNT/graphene electrode. When the thickness of the porous CNT/graphene film is increased from ~ 20 to ~ 80 nm, r increases from ~ 5 to ~ 50 (Fig. 1, D and E). As we will see later in the text, this trend reflects the degree of absorption of Cl^- counterions in high-capacitance (~ 180 F/g; see fig. S1, C and D), equipotential CNT/graphene films (11, 12). We observe that despite having no “p-n” junction or intrinsic internal electric field (13), the rectification ratios in our devices are ~ 5 to 10 times higher than in diodes formed by laminating thin layers of oppositely charged AuTMA and AuMUA NPs (8). These ratios are achieved within tens of milliseconds upon reversal of bias (Fig. 2A), that is, on time scales comparable to conductive polymers (14, 15) but significantly slower than microseconds for Si-based diodes, and are then stable for as long as 50 days (Fig. 2, B and C, and fig. S2B). The diodes that we describe are also mechanically sturdy and continue to operate when bent (see fig. S3).

With our ultimate objective in mind to interface the charged AuTMA NPs with radio signals, we integrated CNT/graphene//Au TMA//Au rectifiers into a half-wave rectification circuit with a single-phase sup-

ply (Fig. 2D). A typical half-wave rectification effect, in which the positive halves are passed while the negative halves are blocked even at kilohertz frequencies, is illustrated in Fig. 2E. We observe that the peak values of output voltage remain unchanged (~ 0.38 V) when frequency increases but are lower than the 1-V input value because the device has internal resistance (approximately megohm with microampere forward current) comparable to the external load (1 megohm). Although the rectification ratios at peak voltages, ± 0.38 V, decrease with frequency exponentially (Fig. 2F), $r = 1.6$ is still maintained at 500 kHz.

On the basis of these characteristics, we assembled a radio wave receiving circuit (Fig. 3A) in which the audio signal (generated by iPhone; Fig. 3B, left) carried by a 510-kHz amplitude modulation (AM) radio wave (produced by the homemade transmitting circuit; Fig. 3B, middle) was intercepted, demodulated, and finally converted into the sound signal by the receiving circuit on the basis of the CNT/graphene//Au TMA//Au rectifier (Fig. 3B, right). Two audio waveforms were recorded (Mozart's Turkish March in Fig. 3C and Symphony No. 40 in Fig. 3D; see audio files in the supplementary materials) demonstrating that this system could function as a qualified detector (although sound quality could, no doubt, be improved). In a control experiment, the sound signal disappeared completely when the NP-based rectifier was replaced by a resistor with similar resistance.

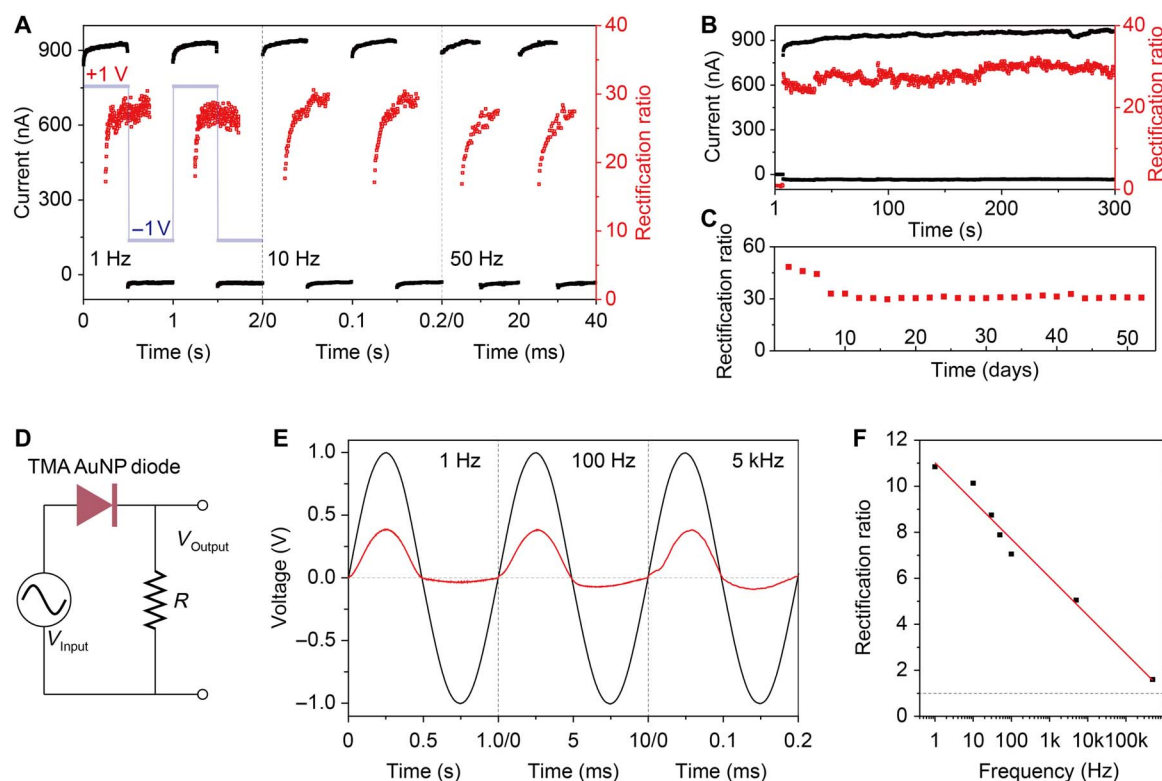


Fig. 2. Time-dependent performance characteristics of AuNP-based rectifiers. (A) Current transients monitored upon inverting the bias from +1 to -1 V at frequencies of 1, 10, and 50 Hz (square wave, light blue curve). Rectification ratios increase to steady-state values within tens of milliseconds (red curve, right axis). (B) Current monitored for 300 s upon stepping the bias from 0 to +1 or -1 V. The rectification ratio is plotted by dividing the currents at +1 and -1 V (red curve, right axis). (C) Rectification ratio quantified over much longer times, up to ~ 50 days. (D) Diagram of a half-wave rectifier circuit composed of a NP-based rectifier, a resistor, and an AC signal generator. (E) Performance of this half-wave rectifier circuit ($R = 1$ megohm) with sinusoidal voltage signals with varying frequencies as inputs (V_{input} , black curve). As frequency increases from 1 to 5000 Hz, the rectification ability diminishes and $|V_{\text{max}}/V_{\text{min}}|$ decreases from ~ 11 to ~ 5 (V_{output} , red curve). (F) The rectification ratio decreases exponentially with increasing frequency, although it is still present at 500 kHz ($r = 1.6$). The thickness of CNT/graphene electrodes used in (A), (B), (C), and (E) is ~ 60 nm.

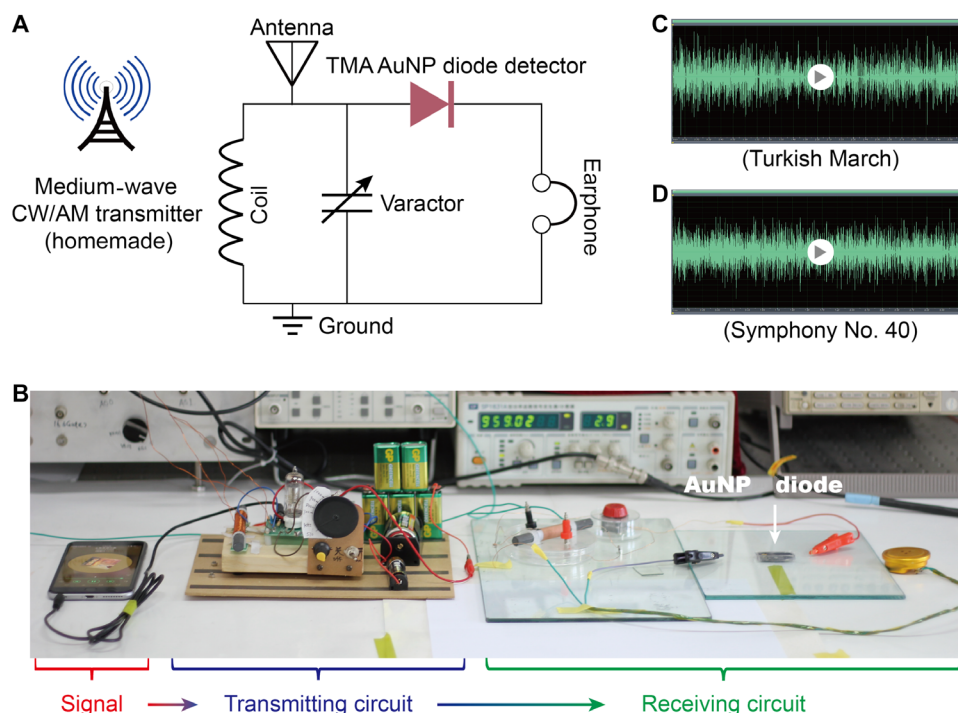


Fig. 3. NP-based radio receiver. (A) Diagram of a radio wave receiving circuit composed of a NP-based diode, an antenna, a varactor, an electromagnetic coil, and an earphone. A one-tube medium-wave continuous wave (CW)/AM transmitter was assembled in-house to generate carrying waves. (B) A photograph of an actual experimental setup in which audio signals carried by a 510-kHz AM radio wave (produced by the transmitting circuit) were intercepted, demodulated, and finally converted into sound by the receiving circuit. (C and D) Examples of two audio waveforms (Mozart's Turkish March and Symphony No. 40) recorded by the NP-based receiving circuit with an ~80-nm-thick CNT/graphene composite electrode. Audio files are included in the supplementary materials. Photo credit: Y. Yan, National Center for Nanoscience and Technology, Chinese Academy of Sciences.

DISCUSSION

Of course, a limitation of the current setup compared to analogous semiconductor devices is that the rectification ratio vanishes for megahertz waves. To elucidate the origin of this limitation, and possibly remedy it, it is important to understand the physical phenomena enabling current rectification. To this end, we adapted a continuum charge transport model combining of Poisson and Nernst-Planck diffusion equations (7). In this model (see section S2 for equations and additional details), both mobile counterions and conduction electrons—but not the jammed NPs—can migrate in response to local electric fields and concentration gradients. However, while the conduction electrons can flow freely in and out of the NP layer at either electrode, the counterions can only move into the CNT/graphene electrode. Moreover, within the NP layer, the motions of ions and electrons are related to each other such as to maintain local charge neutrality. The calculated concentration plots shown in Fig. 4 (A and B) are evidence that mobile counterions migrate into the porous electrode to a significantly larger extent under positive versus reverse bias. This asymmetry is reflected in the differences in the steady-state spatial distributions of conduction electrons (n_e) (Fig. 4C and fig. S5, A and B), potentials (u) (Fig. 4D and fig. S5, C and D), and electric fields (E) (Fig. 4E and fig. S5, E and F). Consequently, it influences transport of electrons between neighboring NPs (see below) and ultimately results in current rectification [see I - V characteristics in Fig. 4F versus Fig. 1 (B and D) and transient current responses in Fig. 4G versus Fig. 2B]. The model also captures the increase in the rectification ratio with increasing thickness of the CNT/graphene electrode (Fig. 4H);

this trend is due to the fact that as more counterions can diffuse into thicker electrodes, the steepness of ionic gradients and the magnitude of the electric field in the NP films both increase (see also fig. S6). For detailed comparison between theory and experiment, see fig. S7.

The asymmetric nature of counterion gradients within AuTMA films postulated by the model was confirmed experimentally by two different techniques: Kelvin force microscopy (KFM) and energy-dispersive x-ray spectroscopy (EDS). Since visualization transverse to the plane of a thin NP film flanked from top and bottom by Au and CNT/graphene electrodes is not possible, we used a planar configuration in which a 500-nm-thick layer of our AuTMA NPs was applied onto a silica substrate (silicon with 500-nm SiO_2 top layer) supporting a wet-transferred CNT/graphene electrode and an e-beam-evaporated Au electrode (Fig. 5A). Figure 5B gives the experimental KFM potential scans in the absence of bias ($V = 0$ V), under constant positive bias applied on the CNT/graphene electrode ($V = +1.0$ V), and under the same magnitude but negative bias applied on CNT/graphene ($V = -1.0$ V). As seen, the KFM scans for the film under bias feature discernible gradients; as quantified in Fig. 5C, the gradient is steeper for $V = +1.0$ V, when negative Cl^- counterions can migrate toward and into the porous CNT/graphene electrode. Consequently, the magnitude of the electric field established inside the film is higher for the $V = +1.0$ V than for the -1.0 -V bias (Fig. 5D). These results agree qualitatively with the theoretical predictions in Fig. 4 (D and E, respectively). Still, the KFM measurements visualize the potential, but they do not provide any information about the chemical nature of the charged species involved in its creation. To unequivocally confirm the

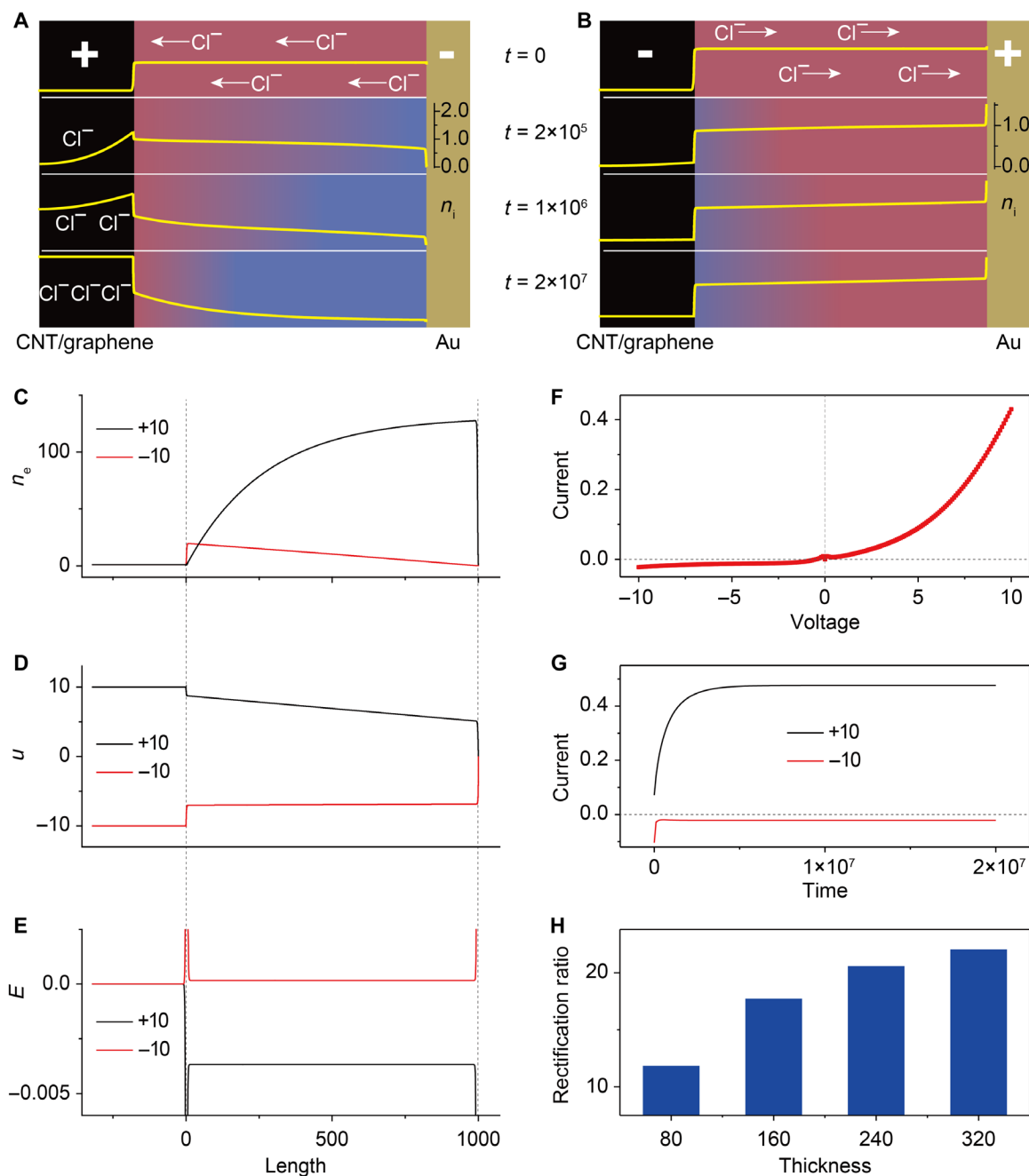


Fig. 4. Theoretical description of the NP-based rectifiers. Time-dependent distribution of Cl^- counterions under positive bias placed on (A) CNT/graphene and (B) Au electrodes. Left: Black, CNT/graphene electrode. Right: dark yellow, Au electrode. Yellow lines, dimensionless concentration profiles of Cl^- as a function of time (from top to bottom, $t = 0, 2 \times 10^5, 1 \times 10^6,$ and 2×10^7). Concentration scale bars are plotted on the Au electrodes. When a positive bias is placed on CNT/graphene, counterions can migrate into this electrode because of its porous and capacitive characteristics. In contrast, with positive bias placed on the Au electrode, counterions cannot enter bulk gold and only accumulate at the electrode's surface. (C) Steady-state distributions of conduction electrons (n_e), (D) electric potential (u), and (E) electric field (E) across the NP layer under positive bias on CNT/graphene (black curves) or Au (red curves) electrodes. Within the NP layer, ions and electrons move in concert to maintain local charge neutrality. (F) Dimensionless steady-state I - V characteristics of the rectifier. (G) Dimensionless time-dependent current characteristics with constant bias placed on either CNT/graphene or Au electrodes. (H) Modeled dependence of the rectification ratio on the thickness of the CNT/graphene electrode. The rectification ratios are quantified by dividing steady-state currents at dimensionless potentials +10 and -10. The dimensionless thickness indicated on the horizontal axis (80 to 320) corresponds to experimental thickness varying from 20 to 80 nm. For further details of the model, see section S2.

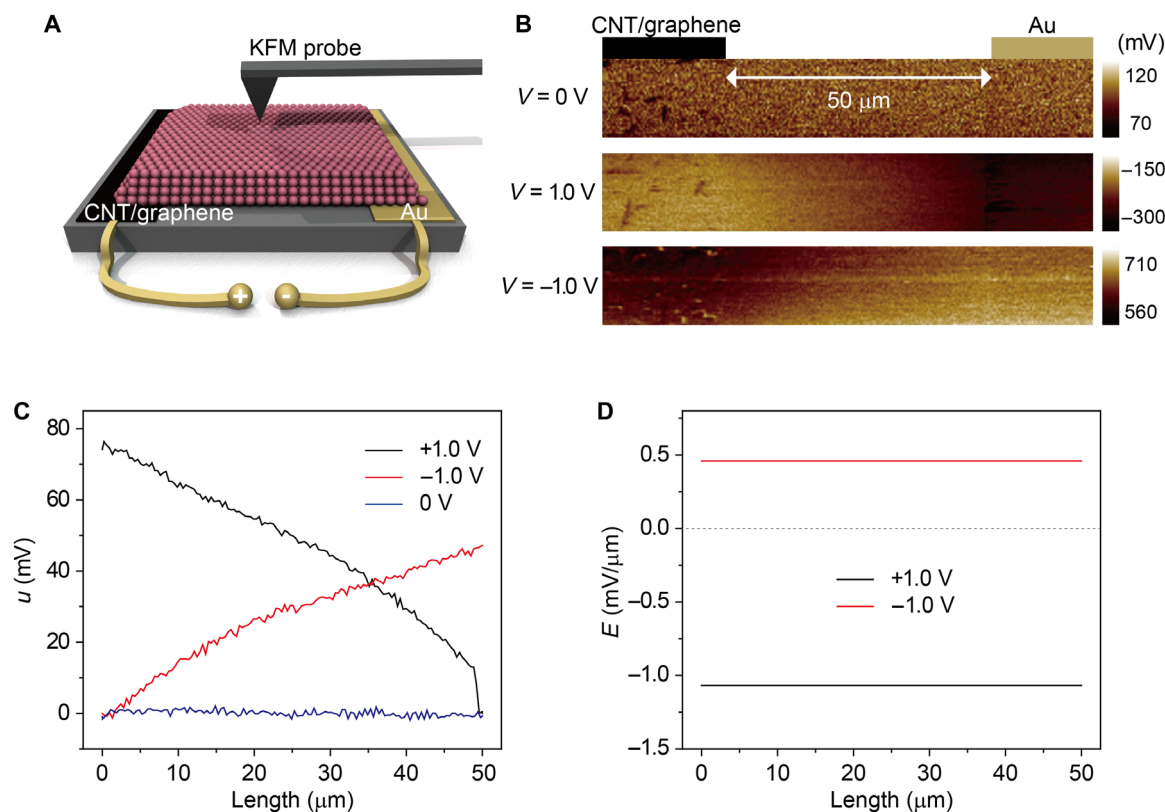


Fig. 5. KFM potential scans over planar AuTMA films. (A) Scheme of the experimental arrangement and (B) actual experimental scans over the 50- μm gap between the CNT/graphene and Au electrodes. (C) Potential profiles over the gap under no bias (0 V, blue line), +1 V bias placed on the CNT/graphene electrode (black line), and -1 V bias on the CNT/graphene electrode (red line). (D) Internal fields derived from the linearly fitted slopes of the profiles in (C). The magnitude of the field established when Cl^- counterions migrate toward and into the CNT/graphene electrode is larger. KFM measurements were performed on a Bruker Multimode-8 in the tapping mode with constant bias applied on CNT/graphene or Au electrodes.

mobility of counterions, we obtained such information from EDS elemental mapping. As shown in Fig. 6, on one hand, there are no systematic gradients in the concentrations of Au and S elements either in the absence or in the presence of bias, that is, the thiol-stabilized NPs do not move. On the other hand, gradients are observed under bias for Cl^- ; again, the gradient for the positive bias placed on the porous CNT/graphene electrode (rightmost image in Fig. 6B) is more pronounced than when the bias is reversed and Cl^- ions migrate toward the Au electrode. More mapping results and accompanying time- and voltage-dependent counterion profiles are included in fig. S8.

Going back to the theoretical model, it predicts $r \sim 20$ as opposed to $r \sim 50$ for 80-nm CNT/graphene electrodes. This discrepancy can be avoided by better accounting for the tunneling current between adjacent NPs. Specifically, according to the so-called Simmons model (16), the tunneling current density through a barrier between two adjacent NP cores can be expressed as $j \propto \exp(-\beta d)$, where β is a structure-dependent attenuation factor and d is the edge-to-edge spacing between AuNP cores. For NPs capped with alkyl thiols, β is typically $\sim 1.0 \text{ \AA}^{-1}$ and d is $\sim 15 \text{ \AA}$ for the TMA AuNPs (based on the core size determined by transmission electron microscopy and lattice size of the NP film by SEM; see also fig. S9, A and B) (8, 17–19). Under forward bias, the steady-state concentration of counterions within the NP layer is reduced by (on average) $\sim 92.8\%$ (Fig. 4A); for the reverse bias, this value is $\sim 26.4\%$ (Fig. 4B). Thus, the barrier height difference can be approximated as $(92.8\% - 26.4\%) * 1 \text{ eV} = 664 \text{ meV}$, corresponding

to $\sim 25.8\%$ difference in β (since $\beta \propto \sqrt{\phi}$, where ϕ is the barrier height) and translating into the ratio of forward and reverse currents of 47.9, that is, close to the experimentally observed rectification ratio of ~ 50 (see also fig. S9, C to F).

CONCLUSIONS AND OUTLOOK

With these theoretical considerations at hand, we consider possible future improvements of the NP-based rectifiers by increasing the rectification ratio and/or by decreasing the “switching times.” For the former, to increase the difference in the steepness of ionic gradients under forward versus reverse biases, one could use electrodes capable of adsorbing more counterions not only by making CNT/graphene films thicker but also by considering other porous, conductive, and high-capacitance materials such as porous carbon composites (20, 21), metallic nanostructures (22), or even metal-organic frameworks (23). One could also increase concentration of counterions either by decreasing NP sizes or by decorating the NPs with polyionic ligands (24, 25). Regarding the switching times, these depend on the time scale of counterions shuttling between two electrodes and scale approximately quadratically with the thickness of an NP layer ($t \propto L^2$) (7). A 10-nm-thick layer would then be expected to exhibit microsecond switching times comparable to silicon diodes. Unfortunately, making these thin NP layers without shorting the planar electrodes flanking them remains challenging. Still, these technical challenges do not seem

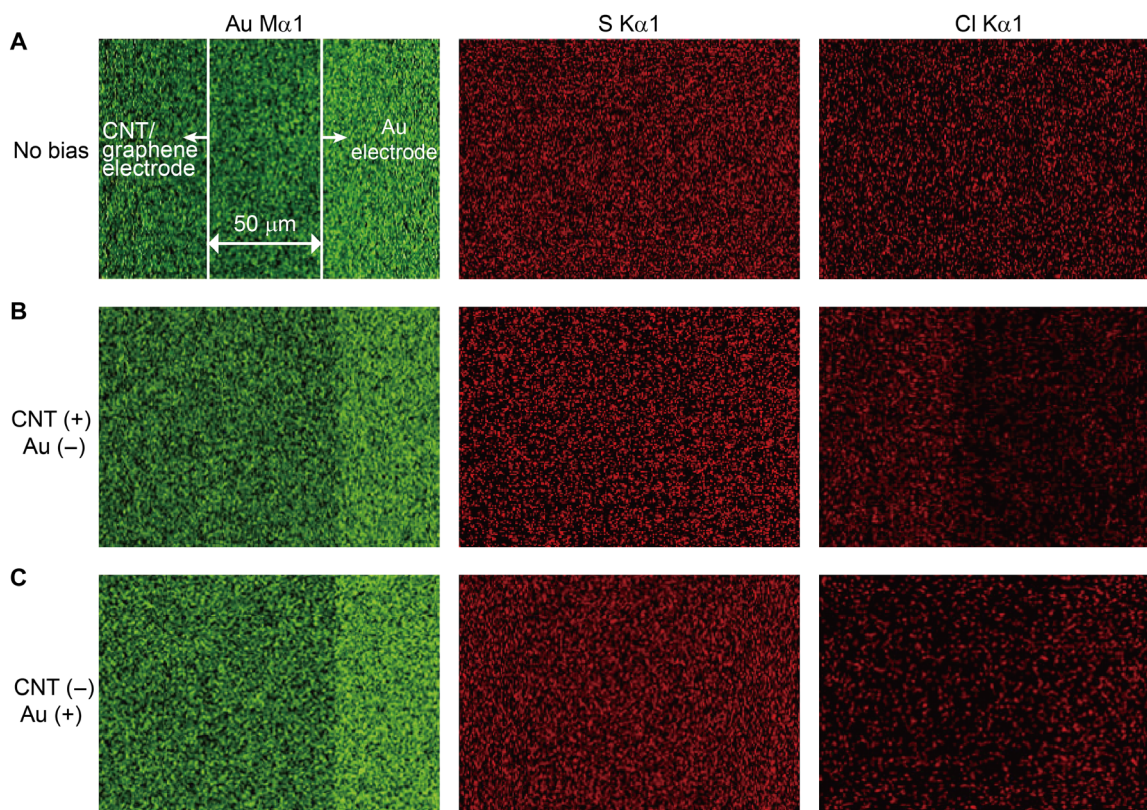


Fig. 6. EDS elemental distribution mapped over planar AuTMA films. The arrangement used for these measurements is the same as in Fig. 5A for KFM. The distribution of Au, S, and Cl under no bias (A), +2-V (100 s) bias applied on the CNT/graphene electrode (B), and +2-V (100 s) bias applied on the Au electrode (C). The intense Au signal at the right parts of Au maps is due to the Au electrode under the NPs. The most pronounced concentration gradient is observed when Cl^- counterions move toward the CNT/graphene electrode [rightmost image in (B)]. Measurements were performed on a Hitachi SU8220 SEM using a Horiba EMAX x-ray detector.

insurmountable. Future effort in this area seems motivated not only by the ability to interface charged NPs with radio waves that we considered here but also with chemical inputs [hence, the “chemoelectronics” term that we coined in (8)]; in particular, faster diodes can significantly accelerate the speeds with which chemoelectronic circuits process chemical inputs (previously on the time scale of only ~ 0.1 to 1 s). In addition, we envision various plasmonic (26), catalytic (27), magnetic (28), or bacteriostatic (29) applications capitalizing on properties unique to metal NPs and hard to achieve with materials used in traditional Si-based electronics.

MATERIALS AND METHODS

NP synthesis and functionalization

Gold NPs were synthesized according to previously reported procedures (6, 9). AuNPs (5.6 ± 0.8 nm) covered with a shell of positively charged TMA ligands were prepared according to the procedure described in detail in section S1.

Fabrication of CNT/graphene electrodes

A vacuum-assisted filtration procedure was applied to fabricate the CNT/graphene electrodes (10). First, 0.002 wt % SWNT solution was prepared by dispersing 2 mg of SWNT powder (>95 wt %) and 4 mg of SDS in 100 ml of deionized (DI) water under probe sonication (150 W, 1 hour). A 0.001 wt % solution of reduced graphene oxide was sonicated in a bath for 10 min. Five milliliters of 0.001 wt % graphene and 5 ml of

0.002 wt % SWNT solutions were then successively filtrated through a polymeric membrane (0.22 μm of MCE). The as-prepared composite film was washed with DI water at least six times and then transferred onto a silica substrate. A few drops of water were added onto the MCE membrane to make the film adhere to the substrate tightly. After evaporation of water, the MCE membrane was peeled off, and the film was then annealed at 300°C (30 min) to remove extra solvent. This protocol produced a composite film of ~ 20 nm in thickness. To prepare thicker films, the volume of SWNT solution was increased while the volume of graphene solution was kept constant.

Device fabrication

Gold electrodes (10 mm by 10 mm by 40 nm, with a 5-nm Cr adhesion layer) were deposited onto a silica substrate by e-beam evaporation through a shadow mask. The solutions of TMA AuNPs were drop casted onto gold and CNT/graphene electrodes separately to form ~ 500 -nm-thick films. The as-prepared films were dried overnight and then laminated together with a face-to-face configuration. To prevent atmospheric humidity from influencing device performance, the devices were encapsulated in PDMS.

KFM and EDS measurements

A AuTMA planar device was fabricated by drop casting a 500-nm NP film on a silica substrate supporting a wet-transferred CNT/graphene electrode and an e-beam-evaporated Au electrode. Both electrodes were 5 mm long, 50 μm wide, and 60 nm high and separated from each other

by a ~50- μm gap. The KFM measurements were performed on a Bruker MultiMode 8 apparatus in the tapping mode. The electrodes were wired out and connected with a Keithley 2636B source meter. In the absence of bias, a selected area of ~95 μm by 20 μm was scanned in high resolution (for ~4 min). The bias was then applied on the CNT/graphene electrode (+1.0 V), and the surface potential measurement was started when the current became stable (~2 min). The same procedure was conducted when the bias was applied on the Au electrode (-1.0 V). However, before applying bias on the Au electrode, the device was left for ~10 min with no bias applied, which was used to equilibrate the counterion gradient.

The device architecture used for EDS measurement was the same as for KFM. The device was first placed on a SEM sample stage. This stage was locked on the SEM holder in the sample exchange chamber. Constant bias was subsequently applied either on the CNT/graphene electrode or the Au electrode. After polarization, the leads were immediately peeled off and the chamber was pumped. Measurements were then performed on a Hitachi SU8220 SEM using a Horiba EMAX x-ray detector.

SUPPLEMENTARY MATERIALS

Supplementary material for this article is available at <http://advances.sciencemag.org/cgi/content/full/4/10/eau3546/DC1>

Section S1. Experimental

Section S2. Theoretical details

Fig. S1. Characterization of the structure, thickness, and electrochemical performance of CNT/graphene electrodes.

Fig. S2. Current-voltage characteristics of a control device and stability test of a NP-based rectifier.

Fig. S3. Current-voltage characteristics of the device upon bending.

Fig. S4. Comparison of the frequency performance of TMA and TMA/MUA AuNP diodes.

Fig. S5. Time-dependent distributions of electrons, electric potentials, and fields.

Fig. S6. Thickness-dependent characteristics of AuNP-based rectifiers.

Fig. S7. Comparisons of theoretically predicted versus experimentally observed characteristics of the diodes.

Fig. S8. Distribution of counterions under bias as a function of time and voltage.

Fig. S9. AuNP film and the energy diagrams of two adjacent NPs.

Table S1. Electrical characteristics of CNT/graphene electrodes.

Audio file S1. Turkish March.

Audio file S2. Symphony No. 40.

References (30–37)

REFERENCES AND NOTES

- S. M. Sze, K. K. Ng, *Physics of Semiconductor Devices* (John Wiley and Sons, 2007).
- M. M. Shulaker, G. Hills, R. S. Park, R. T. Howe, K. Saraswat, H.-S. Philip Wong, S. Mitra, Three-dimensional integration of nanotechnologies for computing and data storage on a single chip. *Nature* **547**, 74–78 (2017).
- S. V. Rotkin, K. Hess, Possibility of a metallic field-effect transistor. *Appl. Phys. Lett.* **84**, 3139–3141 (2004).
- A. V. Butenko, D. Shvarts, V. Sandomirsky, Y. Schlesinger, R. Rosenbaum, Hall constant in quantum-sized semimetal Bi films: Electric field effect influence. *J. Appl. Phys.* **88**, 2634–2640 (2000).
- K. S. Novoselov, A. K. Geim, S. V. Morozov, D. Jiang, Y. Zhang, S. V. Dubonos, I. V. Grigorieva, A. A. Firsov, Electric field effect in atomically thin carbon films. *Science* **306**, 666–669 (2004).
- A. M. Kalsin, M. Fialkowski, M. Paszewski, S. K. Smoukov, K. J. M. Bishop, B. A. Grzybowski, Electrostatic self-assembly of binary nanoparticle crystals with a diamond-like lattice. *Science* **312**, 420–424 (2006).
- H. Nakanishi, D. A. Walker, K. J. Bishop, P. J. Wesson, Y. Yan, S. Soh, S. Swaminathan, B. A. Grzybowski, Dynamic internal gradients control and direct electric currents within nanostructured materials. *Nat. Nanotechnol.* **6**, 740–746 (2011).
- Y. Yan, S. C. Warren, P. Fuller, B. A. Grzybowski, Chemo-electronic circuits based on metal nanoparticles. *Nat. Nanotechnol.* **11**, 603–608 (2016).
- N. R. Jana, X. Peng, Single-phase and gram-scale routes toward nearly monodisperse Au and other noble metal Nanocrystals. *J. Am. Chem. Soc.* **125**, 14280–14281 (2003).
- Z. Wu, Z. Chen, X. Du, J. M. Logan, J. Sippel, M. Nikolou, K. Kamaras, J. R. Reynolds, D. B. Tanner, A. F. Hebard, A. G. Rinzler, Transparent, conductive carbon nanotube films. *Science* **305**, 1273–1276 (2004).
- Q. Cheng, J. Tang, J. Ma, H. Zhang, N. Shinya, L.-C. Qin, Graphene and carbon nanotube composite electrodes for supercapacitors with ultra-high energy density. *Phys. Chem. Chem. Phys.* **13**, 17615–17624 (2011).
- A. Orphanou, T. Yamada, C. Y. Yang, Modeling of a carbon nanotube ultracapacitor. *Nanotechnology* **23**, 095401 (2012).
- W. Shockley, The Theory of *p-n* junctions in semiconductors and *p-n* junction transistors. *Bell Syst. Tech. J.* **28**, 435–489 (1949).
- D. A. Bernards, S. Flores-Torres, H. D. Abruna, G. G. Malliaras, Observation of electroluminescence and photovoltaic response in ionic junctions. *Science* **313**, 1416–1419 (2006).
- C. V. Hoven, H. Wang, M. Elbing, L. Garner, D. Winkelhaus, G. C. Bazan, Chemically fixed *p-n* heterojunctions for polymer electronics by means of covalent B-F bond formation. *Nat. Mater.* **9**, 249–252 (2010).
- J. G. Simmons, Generalized formula for the electric tunnel effect between similar electrodes separated by a thin insulating film. *J. Appl. Phys.* **34**, 1793–1803 (1963).
- A. Zabet-Khosousi, A.-A. Dhirani, Charge transport in nanoparticle assemblies. *Chem. Rev.* **108**, 4072–4124 (2008).
- R. H. Terrill, T. A. Postlethwaite, C. Hsien Chen, C. Duen Poon, A. Terzis, A. Chen, J. E. Hutchison, M. R. Clark, G. Wignall, J. D. Londono, M. Falvo, C. S. Johnson, E. T. Samulski, R. W. Murray, G. Wignall, J. D. Londono, R. H. Terrill, T. A. Postlethwaite, C. Hsien Chen, C. Duen Poon, A. Terzis, A. Chen, J. E. Hutchison, M. R. Clark, G. Wignall, J. D. Londono, R. Superfine, M. Falvo, C. S. Johnson, E. T. Samulski, R. W. Murray, Monolayers in three dimensions: NMR, SAXS, thermal, and electron hopping studies of alkanethiol stabilized gold clusters. *J. Am. Chem. Soc.* **117**, 12537–12548 (1995).
- W. P. Wuelfing, S. J. Green, J. J. Pietron, D. E. Cliffl, R. W. Murray, Electronic conductivity of solid-state, mixed-valent, monolayer-protected Au clusters. *J. Am. Chem. Soc.* **122**, 11465–11472 (2000).
- W. Chen, S. Chen, T. Liang, Q. Zhang, Z. Fan, H. Yin, K. W. Huang, X. Zhang, Z. Lai, P. Sheng, High-flux water desalination with interfacial salt sieving effect in nanoporous carbon composite membranes. *Nat. Nanotechnol.* **13**, 345–350 (2018).
- Z. Sun, J. Zhang, L. Yin, G. Hu, R. Fang, H.-M. Cheng, F. Li, Conductive porous vanadium nitride/graphene composite as chemical anchor of polysulfides for lithium-sulfur batteries. *Nat. Commun.* **8**, 14627 (2017).
- X. Lang, A. Hirata, T. Fujita, M. Chen, Nanoporous metal/oxide hybrid electrodes for electrochemical supercapacitors. *Nat. Nanotechnol.* **6**, 232–236 (2011).
- D. Sheberla, J. C. Bachman, J. S. Elias, C.-J. Sun, Y. Shao-Horn, M. Dincă, Conductive MOF electrodes for stable supercapacitors with high areal capacitance. *Nat. Mater.* **16**, 220–224 (2017).
- P. Wang, C. N. Moorefield, K.-U. Jeong, S.-H. Hwang, S. Li, S. Z. D. Cheng, G. R. Newkome, Dendrimer-metallomacrocyclic composites: Nanofiber formation by multi-ion pairing. *Adv. Mater.* **20**, 1381–1385 (2008).
- G. Ou, L. Xu, B. He, Y. Yuan, Enhanced stability of charged dendrimer-encapsulated Pd nanoparticles in ionic liquids. *Chem. Commun.* 4210–4212 (2008).
- Y. Montelongo, D. Sikdar, Y. Ma, A. J. S. McIntosh, L. Velleman, A. R. Kucernak, J. B. Edle, A. A. Kornyshev, Electro-tunable nanoplasmonic liquid mirror. *Nat. Mater.* **16**, 1127–1135 (2017).
- X. Huang, Z. Zhao, L. Cao, Y. Chen, E. Zhu, Z. Lin, M. Li, A. Yan, A. Zettl, Y. Morris Wang, X. Duan, T. Mueller, Y. Huang, High-performance transition metal-doped Pt₃Ni octahedra for oxygen reduction reaction. *Science* **348**, 1230–1234 (2015).
- S. H. Sun, C. B. Murray, D. Weller, L. Folks, A. Moser, Monodisperse FePt nanoparticles and ferromagnetic FePt nanocrystal superlattices. *Science* **287**, 1989–1992 (2000).
- A. P. Richter, J. S. Brown, B. Bharti, A. Wang, S. Gangwal, K. Houck, E. A. Cohen Hubal, V. N. Paunov, S. D. Stoyanov, O. D. Velev, An environmentally benign antimicrobial nanoparticle based on a silver-infused lignin core. *Nat. Nanotechnol.* **10**, 817–823 (2015).
- K. H. An, W. S. Kim, Y. S. Park, J.-M. Moon, D. J. Bae, S. C. Lim, Y. S. Lee, Y. H. Lee, Electrochemical properties of high-power supercapacitors using single-walled carbon nanotube electrodes. *Adv. Funct. Mater.* **11**, 387–392 (2001).
- M. B. Cortie, A. I. Maarouf, G. B. Smith, Electrochemical capacitance of mesoporous gold. *Gold Bull.* **38**, 14–22 (2005).
- J. Jortner, R. M. Noyes, Some thermodynamic properties of hydrated electron. *J. Phys. Chem.* **70**, 770–774 (1966).
- J. Schnitker, P. J. Rossky, Quantum simulation study of the hydrated electron. *J. Chem. Phys.* **86**, 3471–3485 (1987).
- C.-G. Zhan, D. A. Dixon, The nature and absolute hydration free energy of the solvated electron in water. *J. Phys. Chem. B* **107**, 4403–4417 (2003).
- V. B. Engelkes, J. M. Beebe, C. D. Frisbie, Length-dependent transport in molecular junctions based on SAMs of alkanethiols and alkanedithiols: Effect of metal work function and applied bias on tunneling efficiency and contact resistance. *J. Am. Chem. Soc.* **126**, 14287–14296 (2004).

36. T. Lee, W. Wang, J. F. Klemic, J. J. Zhang, J. Su, M. A. Reed, Comparison of electronic transport characterization methods for alkanethiol self-assembled monolayers. *J. Phys. Chem. B* **108**, 8742–8750 (2004).
37. H. Nakanishi, K. J. M. Bishop, B. Kowalczyk, A. Nitzan, E. A. Weiss, K. V. Tretiakov, M. M. Apodaca, R. Klajn, J. Fraser Stoddart, B. A. Grzybowski, Photoconductance and inverse photoconductance in films of functionalized metal nanoparticles. *Nature* **460**, 371–375 (2009).

Acknowledgments: We thank B. Lu for helpful discussions and support on modeling.

Funding: This work was supported by the National Natural Science Foundation of China (21571039) and the Chinese Academy of Sciences. B.A.G. acknowledges support from the Korean Institute for Basic Science, IBS, under project code IBS-R020-D1. **Author contributions:** X.Z. carried out the experiments and, with M.L., X.F., Y.Z., and T.L., performed the data analysis. B.T. and Q.F. modeled the experimental results.

All authors wrote the manuscript. Y.Y. and B.A.G. conceived and supervised the project.

Competing interests: The authors declare that they have no competing interests.

Data and materials availability: All data needed to evaluate the conclusions in the paper are present in the paper and/or the Supplementary Materials. Additional data related to this paper may be requested from the authors.

Submitted 1 June 2018

Accepted 5 September 2018

Published 12 October 2018

10.1126/sciadv.aau3546

Citation: X. Zhao, B. Tu, M. Li, X. Feng, Y. Zhang, Q. Fang, T. Li, B. A. Grzybowski, Y. Yan, Switchable counterion gradients around charged metallic nanoparticles enable reception of radio waves. *Sci. Adv.* **4**, eaa03546 (2018).

Switchable counterion gradients around charged metallic nanoparticles enable reception of radio waves

Xing Zhao, Bin Tu, Mengyao Li, Xiaojing Feng, Yuchun Zhang, Qiaojun Fang, Tiehu Li, Bartosz A. Grzybowski and Yong Yan

Sci Adv 4 (10), eaau3546.
DOI: 10.1126/sciadv.aau3546

ARTICLE TOOLS <http://advances.sciencemag.org/content/4/10/eaau3546>

SUPPLEMENTARY MATERIALS <http://advances.sciencemag.org/content/suppl/2018/10/05/4.10.eaau3546.DC1>

REFERENCES This article cites 35 articles, 6 of which you can access for free
<http://advances.sciencemag.org/content/4/10/eaau3546#BIBL>

PERMISSIONS <http://www.sciencemag.org/help/reprints-and-permissions>

Use of this article is subject to the [Terms of Service](#)

Science Advances (ISSN 2375-2548) is published by the American Association for the Advancement of Science, 1200 New York Avenue NW, Washington, DC 20005. 2017 © The Authors, some rights reserved; exclusive licensee American Association for the Advancement of Science. No claim to original U.S. Government Works. The title *Science Advances* is a registered trademark of AAAS.